A new approach for reverse analyses in depth-sensing indentation using numerical simulation

J.M. Antunes [a,*], J.V. Fernandes [b], L.F. Menezes [b], B.M. Chaparro [a]

[a] *Escola Superior de Tecnologia de Abrantes, Instituto Politécnico de Tomar, Rua 17 de Agosto de 1808, 2200 Abrantes, Portugal*
[b] *CEMUC – Departamento de Engenharia Mecânica – Faculdade de Ciências e Tecnologia, Polo 2 da Universidade de Coimbra –
Pinhal de Marrocos, P-3030-201 Coimbra, Portugal*

Abstract

This paper seeks to present a new approach to reverse analysis in depth-sensing indentation which makes use of numerical simulation. This methodology allows the results of experimental hardness tests acquired with single indenter geometry to be used to determine the plastic properties of materials. Forward and reverse analyses of high deformation three-dimensional numerical simulations of Vickers indentation tests are used to determine different mechanical properties of materials: Young's modulus, yield stress and strain-hardening exponent. The Vickers indenter used in the numerical simulations is formulated as a rigid body and takes into account the presence of the most common imperfection of the tip, so-called offset. The contact friction between the Vickers indenter and the deformable body is also considered. The forward analysis uses materials with Young's modulus values from 50 to 600 GPa, yield stress values from 0.3 to 10 GPa and strain-hardening exponents from 0 to 0.6; the Poisson ratio did not vary from 0.3. The representative plastic strain ε_r and the correspondent stress σ_r, as previously defined by other authors [Dao M, Chollacoop N, Vliet KJ, Venkatesh TA, Suresh S. Acta Mater 2001;49:3899], were identified by an independent numerical method. The values of the representative plastic strain ε_r obtained for the Vickers indenter confirm those of the above-mentioned authors, despite showing a slight influence from the Young's modulus values. The forward study enables the production of a unique plot of the hardness H_{IT} vs. representative stress σ_r, where both are normalized by the Young's modulus E. The proposed reverse analysis provides a unique solution to the representative stress σ_r and the strain-hardening exponent, n, given that the Young's modulus is predetermined from the experimental hardness test. Depending on the material properties, the value of n can be more or less sensitive to the scatter of the experimental results obtained using the depth-sensing equipment, particularly the stiffness of the unloading curve. The validity of the proposed reverse analysis method is checked using three real materials: stamping quality steel (DC 06), stainless AISI 304 steel and BK7 glass.

1. Introduction

Indentation tests are commonly used in the evaluation of the mechanical properties of bulk and coated materials. Depth-sensing indentation can be used not only for the evaluation of hardness, but also in the determination of other mechanical properties such as Young's modulus, stress–strain curves and residual stress (e.g. [1–9]).

To successfully use indentation methods for the mechanical characterization of materials, a precise understanding of the correlations between stress–strain and indentation load–unloading curves is required. From experimental data of copper and mild steel with different strain hardening, Tabor [10] proposes one such fundamental correlation. The correlation states that in a large domain hardness is proportional to uniaxial stress, at a representative plastic strain of 0.08, that is:

$$H_{IT} = D\sigma_r \tag{1}$$

* Corresponding author. Tel.: + 351 239 790700; fax: + 351 239 790701.
E-mail address: jorge.antunes@dem.uc.pt (J.M. Antunes).

where H_{IT} is the hardness of the material, D is a proportionality constant and σ_r is the stress corresponding to the representative plastic strain, ε_r, whose value is 0.08 in the case of the Vickers indenter, Tabor found the constant D equal to 3.3 [10]. Later, Johnson [7] concluded that the ratio between the hardness and the representative stress of elastic–plastic materials is governed by the single parameter $(E/\sigma_r)\tan\alpha$, where α is the angle of inclination of the face of the indenter to the surface of the sample, E is the elastic modulus of the material and σ_r is the stress associated with the representative plastic strain, ε_r, which depends on the α angle: $\varepsilon_r = 0.2\tan\alpha$.

Subsequently, a large number of numerical and experimental studies have been conducted towards the aim of fully understanding representative plastic strain and the strain field around indentations, as well as of correlating stress–strain with indentation load–unloading curves (e.g. [11–19]). Different values of the representative plastic strain, ε_r, were proposed as a function of the geometry of the indenter (e.g. [12,13,15–17]). Recent studies have proposed a representative plastic strain definition, for specific indenter geometries, which is independent of the strain-hardening exponent [18,19]. These studies have shown that materials with the same Young's modulus and representative stress values present similar indentation–loading curves, whatever the value of the strain-hardening exponent. All these studies show that the definition of representative plastic strain is still a fundamental question that requires careful investigation.

In recent years, efforts have been made to establish a reverse analysis algorithm for the evaluation of the plastic mechanical properties of materials. One of the principal developments in this investigation area is related to the application of the finite element method. many studies of numerical simulations of hardness tests, e.g. [12,16,18,20] were conducted using conical indenters equivalent to Vickers and Berkovich pyramids (apical angle of cone: 70.3°). Methods in which the strain-hardening exponent and yield stress are determined using the indentation curve are still not perfect. Some of their problems stem from experimental inaccuracies. Others are related to the non-uniqueness of reverse analysis in some particular cases, such as when materials with different mechanical properties generate similar indentation load–unloading curves (e.g. [19,20]). In these cases, the non-uniqueness can be solved by using load–unloading curves obtained in experimental tests with two or more indenters with different apical angles [20]. However, this procedure suffers from a natural complicating factor: two or more indenter geometries are needed.

The main objective of this study is to present a numerical method for predicting the stress–plastic strain curves of elastic–plastic materials using the experimental indentation load–unloading curve obtained with a single geometry indenter. For this purpose, forward analysis was applied to the results of the three-dimensional numerical simulations of Vickers hardness tests of several materials with different mechanical properties. Reverse analysis investigates

the uniqueness of the method, particularly in cases for which the former analytical methods can lead to non-uniqueness in the determination of the strain-hardening exponent ($\sigma_y/E \geqslant 0.03$ and $n \geqslant 0.3$ [18]). The accuracy and sensitivity of the proposed reverse analysis method were also examined, taking into account experimental scatter, in the particular cases of three materials, two steels (DC 06 and AISI 304) and a glass (BK7).

2. Finite element simulation

Numerical simulations were performed using the HAFILM home code. This code was specifically developed to simulate hardness tests with any type of indenter shape taking into account contact with friction between the indenter and the sample [21]. The mechanical model that is the basis of the HAFILM code considers the hardness test as a quasi-static process that occurs in the domain of large deformation problems. The core of the code was developed in the early 1990s and it has since been applied with success to the simulation of sheet metal forming processes [21]. HAFILM began development in 1999 [22,23] and since then the code has been continuously upgraded. Today it is a freeware virtual laboratory in the field of depth-sensing indentation tests.

The plastic behaviour of the material is described by the general yield condition:

$$f(\bar{\sigma},\sigma) = \bar{\sigma} - \sigma = 0 \tag{2}$$

In this equation σ is the flow stress in tension, which is a function of isotropic work-hardening, described in this study by the Swift equation:

$$\bar{\sigma} = K\left(\varepsilon_0 + \bar{\varepsilon}_p\right)^n \tag{3}$$

where K, ε_0 and n are constants for a particular material, determined by classical mechanical tests, and $\bar{\varepsilon}_p$ is the equivalent plastic strain. In Eq. (2), $\bar{\sigma}$ is the equivalent stress defined by the plastic yield criterion. In this study, the material is assumed to be isotropic and its plastic behaviour is simply described by the Von Mises yield criterion.

One of the most common difficulties with the numerical simulation of the indentation process is related to the time dependence of the boundary conditions due to the contact with friction between the indenter, assumed as rigid, and the deformable body. In HAFILM, the contact with friction problem is modelled using a classical Coulomb law. To associate the static equilibrium problem with the contact with friction, an augmented Lagrangean method is applied to the mechanical formulation. This leads to a system of non-linear equations, where the kinematic (material displacements) and static variables (contact forces) are the final unknowns of the problem [24]. In order to solve it, the code makes use of a fully implicit Newton–Raphson type algorithm. All non-linearities, induced by the elastoplastic behaviour of the material and by the contact with friction, are treated in a single iterative loop [21]. The friction
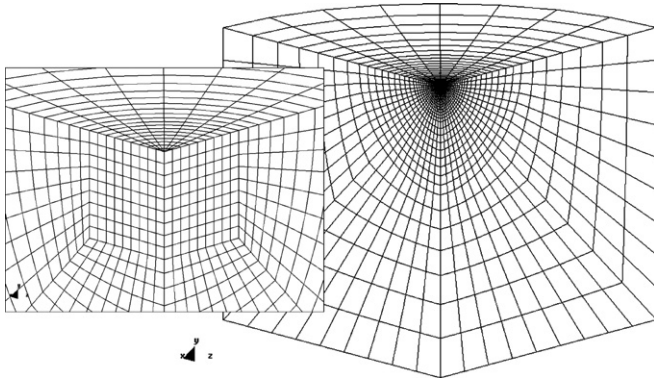
Fig. 1. Finite element mesh used in the numerical simulations.

between the indenter and the deformable body was assumed to have a friction coefficient equal to 0.16. This is a commonly used value and leads to a better description of the indentation process than if frictionless contact were assumed [25].

In the simulations, it was assumed that the Vickers indenter had an indenter tip imperfection: a rectangular planed area (with one side twice the length of the other) with an area of 0.0288 μm^2 was used instead of the ideal tip [25]. This indenter tip imperfection is similar to that of the experimental Vickers indenter tip used in this study, which was measured using atomic force microscopy [26]. Bézier surfaces were used to describe the indenter geometry considered in the numerical simulations. These surfaces allow fine description of the indenter tip.

The sample was discretized into isoparametric solid finite elements associated with a selective reduced integration method that enables the elements performance to improve when large deformations are assumed. Due to geometrical symmetry in the $x = 0$ and $z = 0$ planes, only a quarter of the sample was used in the numerical simulations (Fig. 1). The finite element mesh was composed of 5832 three-linear eight-node isoparametric hexahedrons. Previous studies of the sensitivity of the mesh have improved its performance significantly, guaranteeing reliable estimation of the indentation contact area [25].

3. Representative plastic strain and stress

In a recent study, Dao et al. [18] proposed a group of six dimensionless functions, Π, that relate the characteristic parameters of indentation load–unloading curves to the mechanical properties obtained from the stress–strain curves [18]. One of these functions relates the ratio between the constant of Kick's law, generally used to describe the indentation–loading curve, and the representative stress (k/σ_r) as a function of the ratio between the reduced Young's modulus and the representative stress (E_r/σ_r). The dimensionless function, Π_1, is written thus [18]:

$$\frac{k}{\sigma_r} = \Pi_1\left(\frac{E_r}{\sigma_r}, n\right) \qquad (4)$$

where n is the strain-hardening exponent of the stress–strain curve and the reduced Young's modulus E_r is given by: $1/E_r = (1 - v_s^2)/E + (1 - v_i^2)/E_i$, where E and E_i are the Young's modulus and v_s and v_i are the Poisson ratios of the material and the indenter, respectively. k is the curvature of the loading curve:

$$F = kh^2 \qquad (5)$$

where F is the load and h is the correspondent indentation depth.

Eq. (4) depends on the strain-hardening exponent. However, in the case of a conical indenter with an apical angle of 70.3° (which produces, at a given depth, the same projected area as the Berkovich and Vickers indenters), it was observed that when the representative stress σ_r corresponds to a representative plastic strain value, ε_r, of 0.033, the dimensionless function, Π_1, becomes independent of the strain-hardening exponent [18]. In this context, it appears that materials with the same reduced Young's modulus and representative stress values (corresponding to a representative plastic strain equal to 0.033) present similar indentation–loading curves.

In this study, the value of the representative plastic strain was determined by the comparison of the indentation–loading curves obtained in the numerical simulation of the hardness test of materials with different values of strain-hardening exponents, n, for several values of representative plastic strain (Fig. 2). The true stress–true strain plastic behaviour of the materials used in the numerical simulations was modelled using a Swift-type power law (Eq. (3)). The constant ε_0 was fixed at 0.005. The Young's modulus values, E, were in the range 50–600 GPa and the Poisson ratio, v_s, was equal to 0.3. Stress corresponding to representative plastic strain was considered equal to 0.3, 1, 2, 2.5, 2.75, 3 and 10 GPa. Fig. 2 illustrates the true
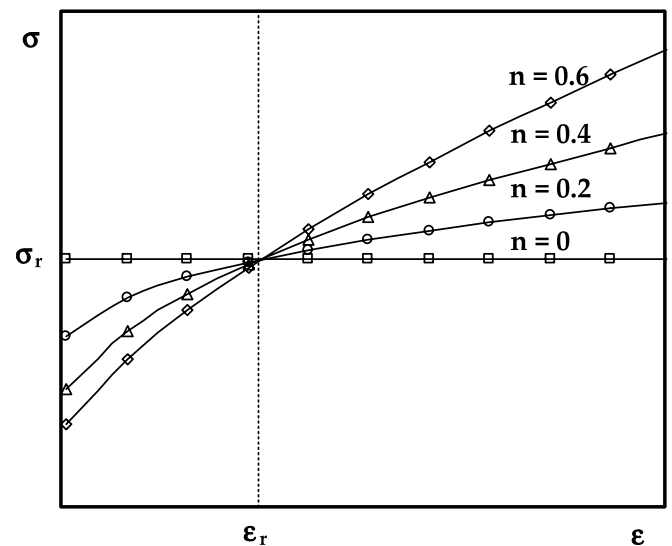

Fig. 2. Schematic description of stress–plastic strain curves, showing the representative strain (ε_r) and the representative stress (σ_r) for the strain-hardening exponents (n) studied.
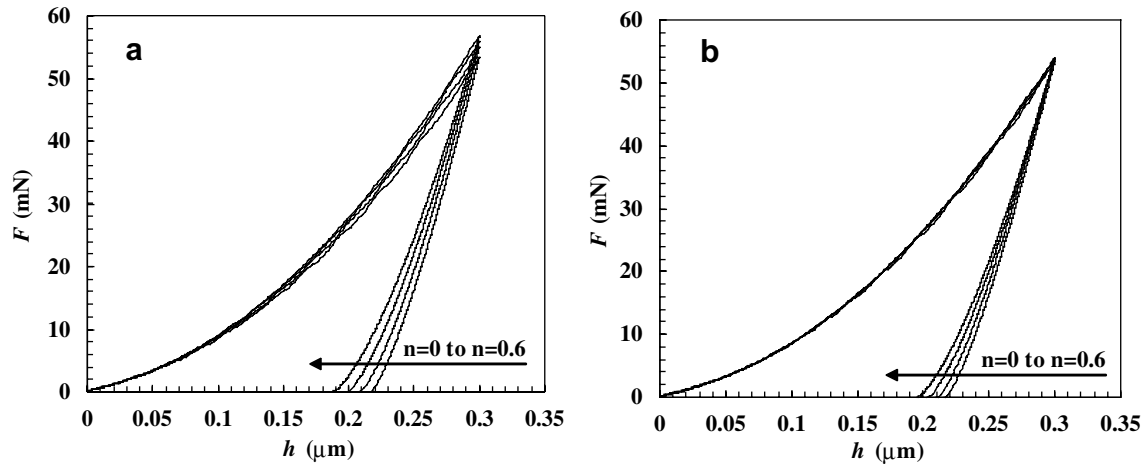
Fig. 3. Load–penetration depth curves obtained by numerical simulations of four materials with different strain-hardening exponents ($n = 0$, 0.2, 0.4 and 0.6), the same values of the reduced Young's modulus ($=450$ GPa) and representative stress ($=10$ GPa). (a) Representative plastic strain ($=0.033$). (b) Representative plastic strain ($=0.042$).

stress–true plastic strain curves of the modulated materials, for four values of the strain-hardening exponent: $n = 0$, 0.2, 0.4 and 0.6. Numerical simulations of the Vickers hardness tests were performed up to a maximum indentation depth equal to 0.3 μm.

In order to begin the forward analysis, the indentation–loading curves of the materials described in Fig. 2 (with four different strain-hardening exponents: $n = 0$, 0.2, 0.4 and 0.6, respectively) were simulated assuming the representative plastic strain to be 0.033, a value proposed by Dao et al. [18]. However, the loading curves relative to materials having a representative plastic strain value of 0.033 are not always similar, as shown in Fig. 3a for the case of a material whose Young's modulus was 410 GPa and whose representative stress was 10 GPa. This fact is probably related to the conditions under which numerical simulation of the hardness tests was performed. Dao et al. [18] established the 0.033 value after a series of numerical simulations with a conical indenter, but did not consider contact friction. Moreover, these authors use a slightly different method to determine the representative strain value: $\varepsilon_r = 0.033$ corresponds to the representative plastic strain value for which the best fit is found for the function Π_1, independently of the strain-hardening exponent n.

In this study, a Vickers indenter was used in three-dimensional numerical simulations that considered friction between the indenter and the sample. Using a trial-and-error process, different values of representative strain were used until coincident loading curves were obtained independently of the strain-hardening exponent, such as exemplified in Fig. 3b. This figure shows the load–unloading curves for a representative plastic strain equal to 0.042 and the strain-hardening exponents of 0, 0.2, 0.4 and 0.6 for materials with a reduced Young's modulus of 450 GPa and a representative stress of 10 GPa. The study carried out on materials with different values of the reduced Young's modulus, from 55 to 660 GPa, and of representa-

tive stress, in the range 0.3–10 GPa, shows that the value of the representative plastic strain depends slightly on the values of the reduced Young's modulus and the representative strain, as shown in Fig. 4. For each case of representative stress, the evolution of representative plastic strain as a function of the Young's modulus can be plotted quite accurately using two straight lines. For values of the reduced Young's modulus in the range 55–450 GPa, the representative strain slightly increases from a minimum of 0.034 up to a maximum value of 0.042 depending on the representative stress, which is equal to or greater than 3 GPa. In each instance of representative stress, σ_r, the representative plastic strain, ε_r, is independent of the reduced Young's modulus, when this is equal to or greater than 450 GPa: ε_r increases, from 0.034 to 0.042, as the representative stress increases towards 3 GPa and remains steady at 0.042 for representative stress values $\geqslant 3$ GPa. A recent investigation
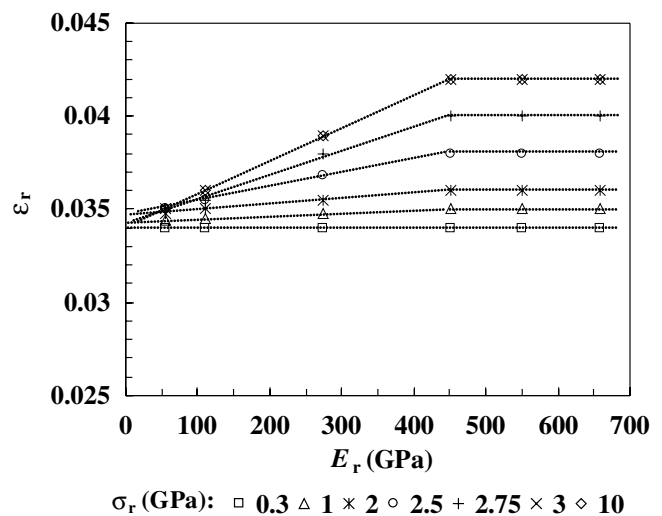

σ_r (GPa): □ 0.3 △ 1 ✳ 2 ○ 2.5 + 2.75 × 3 ◇ 10

Fig. 4. Representative plastic strain (ε_r) vs. the reduced Young's modulus (E_r) for different values of the representative stress: $\sigma_r = 0.3$, 1, 2, 2.5, 2.75, 3 and 10 GPa.

Table 1
Mechanical properties of the various fictitious materials used in the simulations

Materials	Studied cases	n	σ_y (GPa)		E (GPa)	ε_0	v
			Minimum	Maximum			
Without strain hardening	10	≈ 0	0.25	25	100		
	6	≈ 0	0.50	60	410		
With strain hardening	6	0.2	0.15	10	100	0.005	0.29
	6	0.4	0.05	6	100		
	10	0.6	0.05	6	100		
	6	0.6	0.15	6	410		

by Casals and Alcalá [27], using the same methodology as Dao et al. [18] but modelling a Vickers indenter, found a representative strain value of 0.037. This value is close to the middle of the range obtained for representative strain in this study (Fig. 4).

Based on the above analysis, it is possible to establish a relationship between hardness and representative stress. The results obtained from the numerical simulation of Vickers hardness test of several materials with different mechanical properties were used for this purpose. The materials had four values of strain hardening (0, 0.2, 0.4 and 0.6) and two values of reduced Young's modulus: 110 and 450 GPa ($E = 100$ and 410 GPa, respectively, with the Poisson ratio $v_s = 0.3$). The yield stress of the materials, σ_y, was in the range 0.05–60 GPa. Table 1 summarizes the mechanical properties of the materials used for these numerical simulations. The hardness, H_{IT}, was evaluated using the traditional experimental procedure that uses the unloading curve to determine the contact indentation depth, h_c, and consequently the contact area of the indentation. The indentation load–unloading curves had previously been corrected using the area function of the indenter, taking into account the existence of the indenter

tip imperfection [25]. In these curves, the indentation depth, h, corresponds to the depth obtained with an ideal indenter without tip imperfection: $h = \sqrt{A/24.5}$ (where A is the cross-sectional area of the indenter at the surface level of the sample). The representative stress, σ_r, was evaluated using the Swift law for different values of the representative plastic strain, ε_r, as shown in Fig. 4.

Fig. 5 shows that the evolution of hardness as function of representative stress depends on the Young's modulus value. However, for both variables, H_{IT} and σ_r, normalized by the reduced Young's modulus value, the representation of the ratio H_{IT}/E_r vs. σ_r/E_r, becomes independent of the Young's modulus (Fig. 6). Consequently, the representative stress, σ_r, can be estimated from the hardness and the reduced Young's modulus data. Furthermore, the representation of the inverse of the above ratios, E_r/H_{IT} as a function of E_r/σ_r, exhibits linear behaviour (Fig. 7). The linear fitting is expressed by:

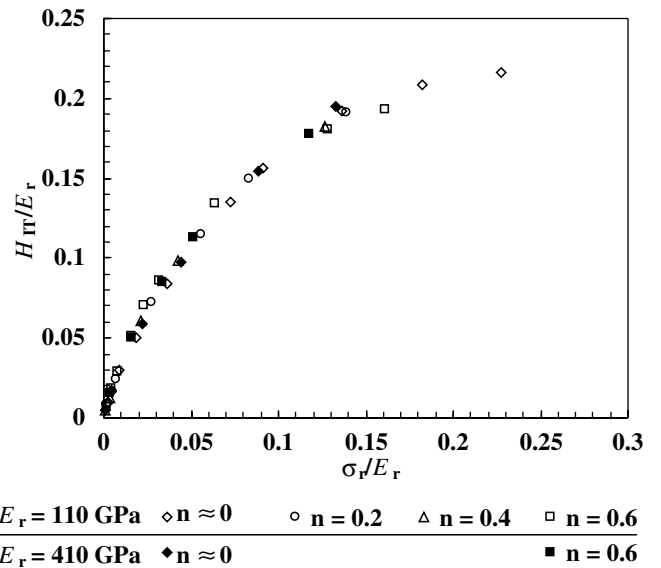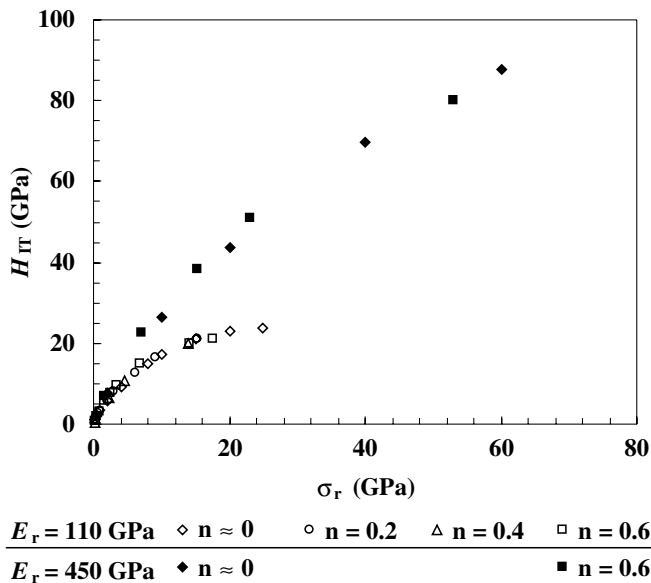$$\frac{E_r}{H_{IT}} = 0.231\left(\frac{E_r}{\sigma_r}\right) + 4.910 \qquad (6)$$

$E_r = 110$ GPa $\diamond$ n ≈ 0 $\circ$ n = 0.2 $\triangle$ n = 0.4 $\square$ n = 0.6
$E_r = 450$ GPa $\blacklozenge$ n ≈ 0 $\blacksquare$ n = 0.6

Fig. 5. Evolution of hardness, H_{IT}, as function of representative stress, σ_r.

$E_r = 110$ GPa $\diamond$ n ≈ 0 $\circ$ n = 0.2 $\triangle$ n = 0.4 $\square$ n = 0.6
$E_r = 410$ GPa $\blacklozenge$ n ≈ 0 $\blacksquare$ n = 0.6

Fig. 6. Evolution of the ratio between the hardness and Young's modulus, H_{IT}/E_r, as function of the ratio between the representative stress and Young's modulus, σ_r/E_r.
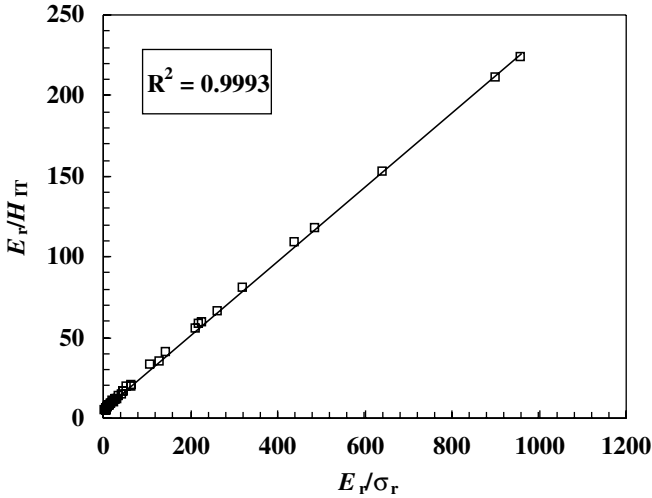
Fig. 7. Evolution of the ratio between the reduced Young's modulus and hardness, E_r/H_{IT}, as function of the ratio between the reduced Young's modulus and the representative stress, E_r/σ_r.

This equation allows representative stress, σ_r, to be easily determined. However, the value of representative stress obtained with this equation may not be accurate enough for some purposes. In such cases, an optimization method should be implemented in order to refine the value.

As discussed above, the hardness loading curves of materials with the same representative stress are independent of the strain-hardening exponent. So an optimization methodology can be established by comparing the experimental and numerical loading curves. To begin the numerical simulation, the material is modulated with the representative stress estimated by Eq. (6), the reduced Young's modulus experimentally determined and an arbitrarily given value of the strain-hardening exponent. If there is a significant difference between the experimental and numerical maximum loads, then representative stress should be optimized using an iterative method, for example:

$$\sigma_r(i+1) = \sigma_r(i)\frac{F_{max}(\exp)}{F_{max}(num)} \qquad (7)$$

where $\sigma_r(i+1)$ and $\sigma_r(i)$ are the $(i+1)$ and (i) order values to be tested, for the representative stress, σ_r, and $F_{max}(\exp)$ and $F_{max}(num)$ are the experimental and numerical maximum loads, respectively. So, each new value of representative stress, $\sigma_r(i+1)$, is followed by a numerical simulation of the loading curve (material modulated with a representative stress equal to $\sigma_r(i+1)$), and then the maximum loads are compared (experimental vs. numerical). The iterative process ends when the ratio between maximum loads,
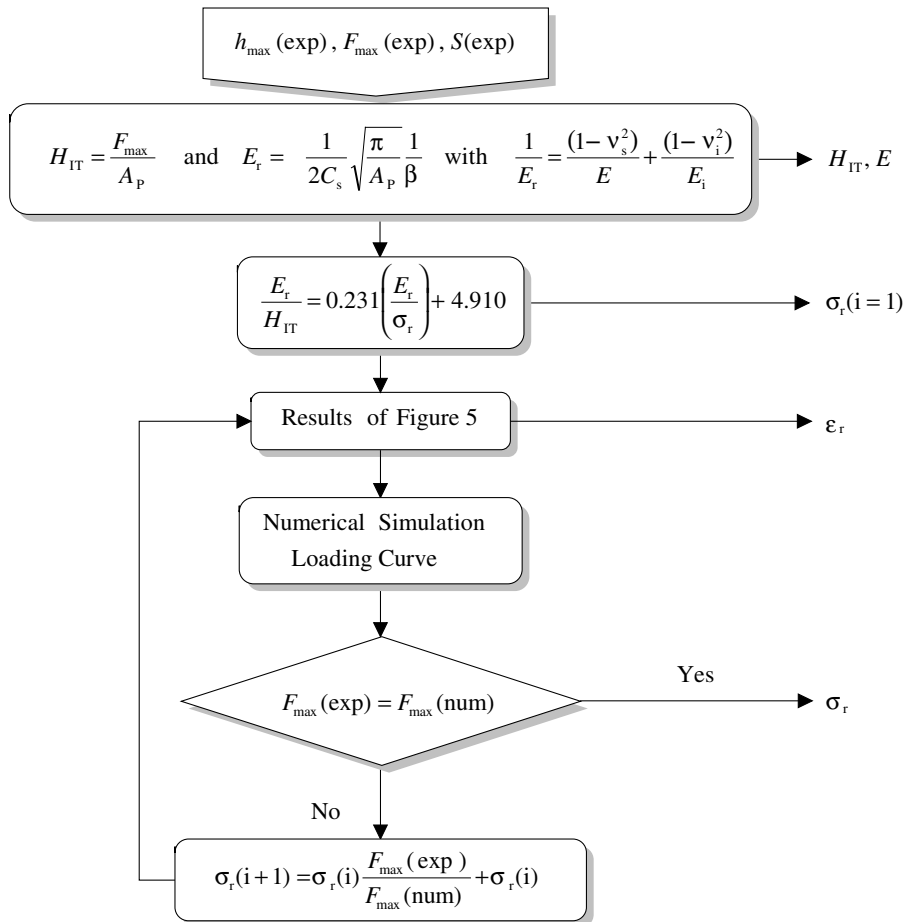

Fig. 8. Reverse analysis algorithm for prediction of the representative plastic strain and stress.
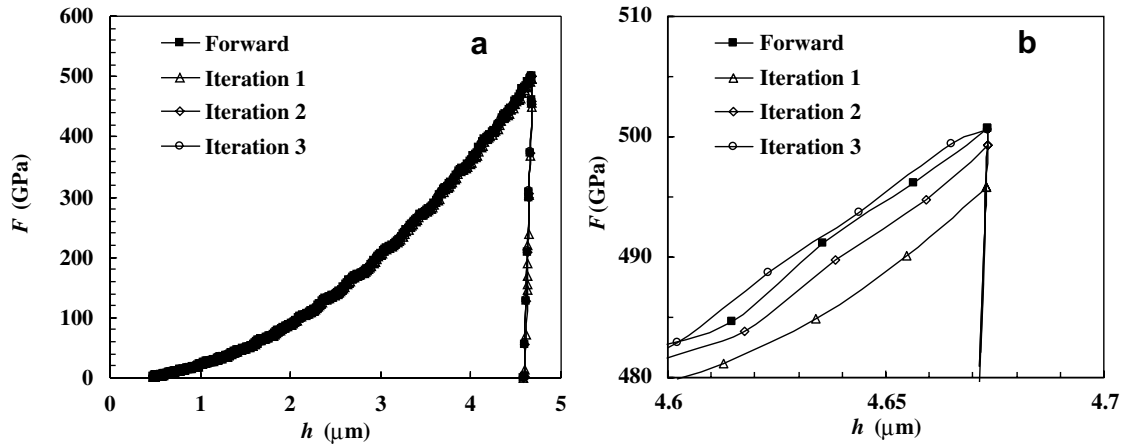
Fig. 9. Example of the use of the reverse analysis algorithm described in Fig. 8, showing forward analysis and three iterations of the load–indentation depth curves: (a) full curves; (b) detail of the upper part of the curves.

experimental and numerical, approximates one. Fig. 8 shows the algorithm that illustrates the iterative procedure for determination of the representative stress.

Fig. 9 shows a numerical example of reverse analysis for determination of representative stress. The forward load–unloading curve (the "experimental" curve in this analysis) was obtained from a material with the following mechanical properties: $E = 200$ GPa and $v_s = 0.3$; the material follows a Swift law relating true stress to the plastic strain logarithm: $\bar{\sigma} = K(\varepsilon_0 + \bar{\varepsilon}_p)^n$, where $K = 0.6$ GPa; $n = 0.3$ and $\varepsilon_0 = 0.005$. From the forward load–unloading curve of this material, we can determine the hardness (0.949 GPa) and the Young's modulus (the value of E determined is within 1% of the input value: $E = 201.6$ GPa). Eq. (6) was used to estimate the starting value of representative stress $\sigma_r(i = 1) = 0.227$ (iteration 1 in Fig. 9b). Therefore, the algorithm in Fig. 8 allows representative stress to be evaluated satisfactorily. After three iterations of the algorithm, similar values at maximum load were obtained (error lower than 0.1%) from both forward and reverse analysis curves, the final value of σ_r being 0.229 GPa. The correspondent characteristic strain obtained from Fig. 4 is 0.034.

4. Strain hardening and yield stress

Most of the reverse analysis methodologies for stress–strain curve prediction based on indentation data make use of complex functions of the strain-hardening exponent. In some cases, no uniqueness is achieved for the value of the strain-hardening exponent. In order to solve this problem, different authors propose the use of load–unloading curves obtained using two or more indenters with different apical angles. This type of procedure has an important drawback, namely the need to prepare and perform experiments with different indenter geometries. To overcome this difficulty, the authors of this study propose a new methodology for evaluating the strain-hardening exponent, using the information contained in the load–unloading curve obtained with single indenter geometry. The basis of the proposed reverse analysis methodology is a careful analysis of the unloading curves obtained by three-dimensional numerical simulations of hardness tests.

The study shows that materials with different values of strain-hardening exponents, but the same Young's modulus and representative stress values, exhibit different behaviours in their unloading curves. In materials with high values of
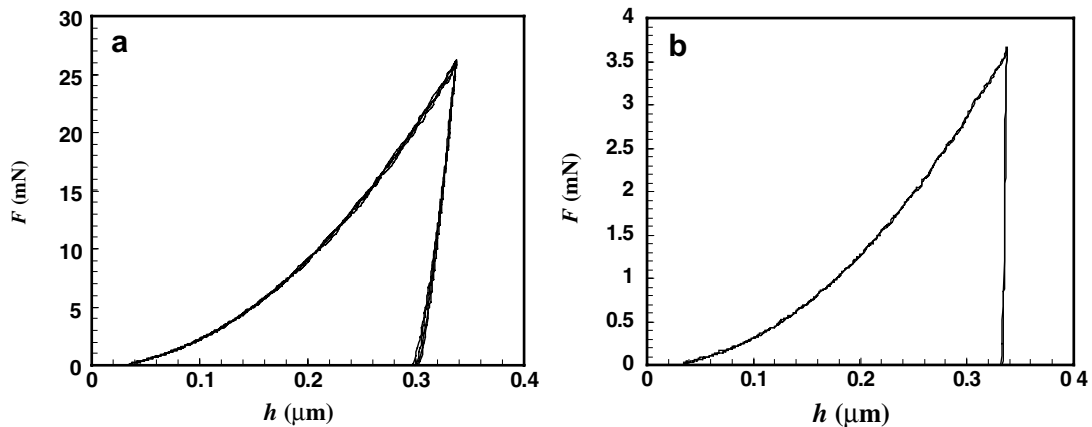

Fig. 10. Numerical indentation responses of materials with Young's modulus equal to 410 GPa and different strain hardening values. The representative stresses are: (a) $\sigma_r = 3$ GPa; (b) $\sigma_r = 0.3$ GPa.
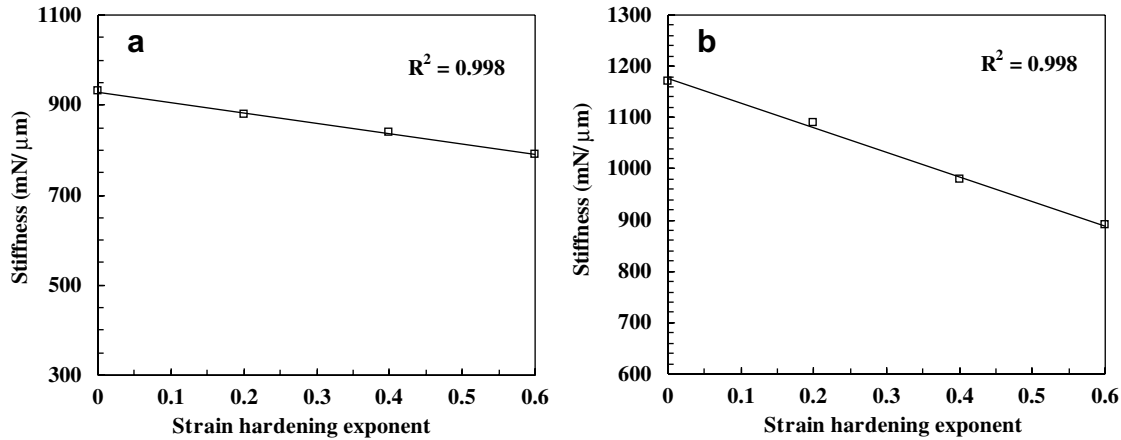
Fig. 11. Stiffness vs. the strain hardening coefficient (open symbols: reverse analysis results; solid symbol: forward analysis). The representative stresses are: (a) $\sigma_r = 3$ GPa; (b) $\sigma_r = 0.3$ GPa.

yield stress (>2.5 GPa), the elastic recovery during unloading indicates a noticeable increase in the strain-hardening exponent, and the comparison of the unloading curves (experimental and numerical) can be adequate enough to predict the strain-hardening exponent (Figs. 3b and 11a). On the other hand, for materials with low yield stress values, the unloading curves become identical, independently of the strain-hardening exponent. In this case, the overall comparison of the unloading curves (experimental and numerical) is not sufficient to obtain a unique value for the strain-hardening exponent (Fig. 10b). However, study of these similar unloading curves, obtained by numerical simulation of materials with different values of strain-

hardening exponent, indicates variation in stiffness, S, evaluated at maximum load ($S = \mathrm{d}F/\mathrm{d}h(h = h_{\max}) = 1/C_t$, where C_t is the total compliance) with the strain-hardening exponent. Following on from Figs. 10 and 11 show the evolution of stiffness as a function of strain hardening. There is a linear decrease in the stiffness as the strain-hardening exponent increases. Therefore, a comparison between experimental and numerical stiffness values ($S_{\exp}$ and S_{num}, respectively) allows the numerical unloading curve that best approaches the experimental to be identified, and from this the n value of the material can be deduced.

The methodology for determining the strain-hardening exponent requires data concerning the Young modulus
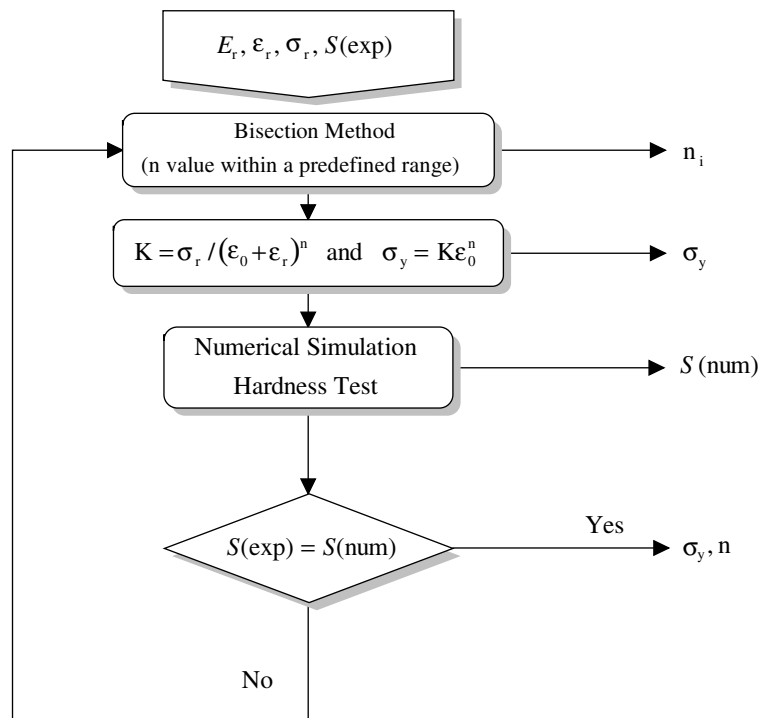

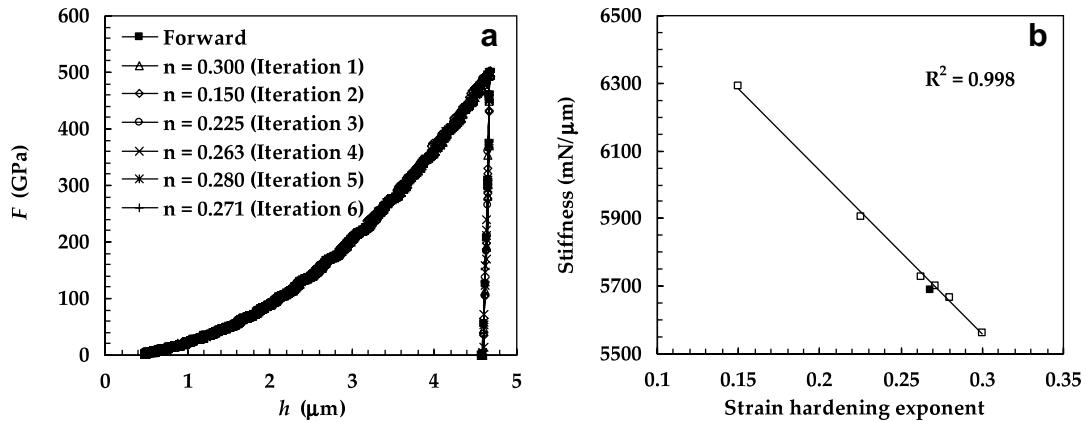Fig. 12. Reverse analysis algorithm for prediction of the strain hardening and yield stress.

Fig. 13. Reverse analysis procedure, using the algorithm shown in Fig. 12: (a) forward and reverse analysis load–indentation depth curves; (b) stiffness vs. strain hardening coefficient (open symbols: reverse analysis results; solid symbol: forward analysis).

and the representative plastic strain and stress, as discussed above (algorithm of Fig. 8). We conclude that the work-hardening coefficient n can be uniquely determined from the slope (stiffness) of the experimental unloading curve (Figs. 11 and 12). Fig. 12 presents the proposed reverse analysis algorithm. Based on an iterative procedure, this reverse analysis begins with the selection of an arbitrary value for the strain-hardening exponent, within an imposed range, and the correspondent value of the yield stress, $\sigma_y = K\varepsilon_0^n$. For the chosen value of the strain-hardening exponent, the correspondent yield-stress value is determined and then both values are used as input data in the numerical simulation of the hardness test. Subsequently, the stiffness of the obtained numerical unload curve, S_{num}, is calculated. The comparison of the experimental and numerical stiffness values, S_{exp} and S_{num}, indicates the accuracy of the approximation. If the difference between S_{num} and S_{exp} is in the range of an imposed maximum error, the process ends, as the mechanical properties used in the numerical simulation approach those of the experimental material. On the other hand, if the difference in stiffness values is too great, the process decides on a new value for the strain-hardening exponent. For this purpose, a classical bisection method was used to select the new strain-hardening exponent, which takes into account the position of the numerical stiffness, S_{num}, in relation to the experimental stiffness, S_{exp}.

The numerical example of reverse analysis used for determination of the representative stress, shown in Fig. 9, is now used for the reverse analysis determination of the strain-hardening coefficient and the yield stress. Fig. 13a shows these load–unloading curves determined for successive iterations of n values in the range 0–0.6. For comparison, the forward load–unloading curve (the "experimental" curve in this analysis) is also shown. This figure gives the impression that the load–unloading curves are apparently independent of the strain-hardening exponent. However, Fig. 13b shows a significant evolution of the stiffness (evaluated from the unloading curves of

Fig. 13a) as a function of the strain-hardening exponent. A straight line can accurately be fitted to the behaviour shown in Fig. 13b. This fact can be used to accelerate the reverse analysis process, by reducing the time used in the numerical simulations. Effectively, two points are enough to describe the linear relationship between the strain-hardening exponent and the stiffness for a specific material. Fig. 13b can also be compared with the "experimental" stiffness result obtained by using the reference mechanical properties of the material and the predictions obtained in each iteration of the reverse analysis algorithm. Fig. 14 presents the corollary of the reverse analysis, the estimation of the experimental stress–strain curve, for the successive iterations. As shown in Fig. 14, the stress–strain curve obtained after six iterations of the reverse analysis algorithm accurately approaches the experimental one. The strain-hardening exponent and the yield stress values obtained after convergence of the reverse analysis algorithm present errors of 6 and 0.73%, respectively.
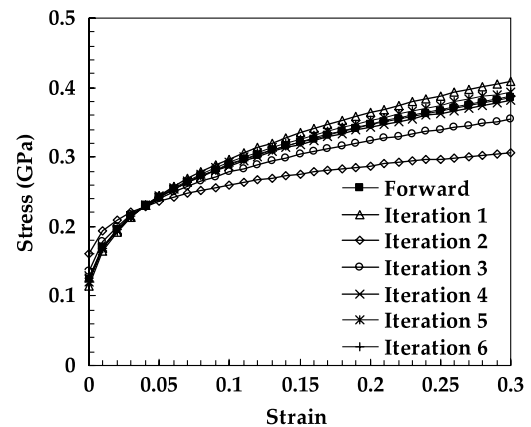

Fig. 14. Stress–plastic strain curves, obtained in forward analysis and after each iteration of the reverse analysis (Fig. 13), during strain hardening coefficient optimization, by using the algorithm shown in Fig. 12.

5. Reverse analysis of real materials

In order to check further the proposed reverse analysis methodology, three real materials were used: stamping quality steel, DC 06, stainless AISI 304 steel and BK7 glass. The true stress–logarithmic plastic strain curves of both steels have been determined using Instrom tensile testing equipment, using a 50 mm extensometer. The tensile tests were performed at a relatively low strain rate of 10^{-3} s^{-1}. Table 2 presents the mechanical properties of these materials (the mechanical properties of the BK7 glass sample have been determined previously [28]).

The full examination of the reverse analysis method was performed using the load–unloading curves obtained in experimental ultramicrohardness tests of the three materials. Experimental hardness tests were performed using the Fischerscope ultramicrohardness equipment and a Vickers indenter. The maximum loads applied were 500 and 100 mN, for the steels (DC 06 and AISI 304) and the BK7 glass, respectively. The correspondent hardness tests were performed at a loading and unloading rate of approximately 1 and 0.2 N/min, respectively. For each material, 25 experimental tests were performed. The experimental curves used in the reverse analysis take into account the thermal drift and the first load point corrections; moreover, the load–unloading curves were also corrected with the area function, taking into account the indenter tip imperfection [26].

Table 2
Mechanical properties of the real materials

Materials	σ_y (GPa)	E (GPa)	v_s	n
DC 06 steel	0.124	200–210	0.30	0.268
AISI 304 steel	0.306	190–200	0.30	0.424
BK7 glass	3.500	82	0.20	0.010

Table 3
Evaluated mechanical properties for the real materials

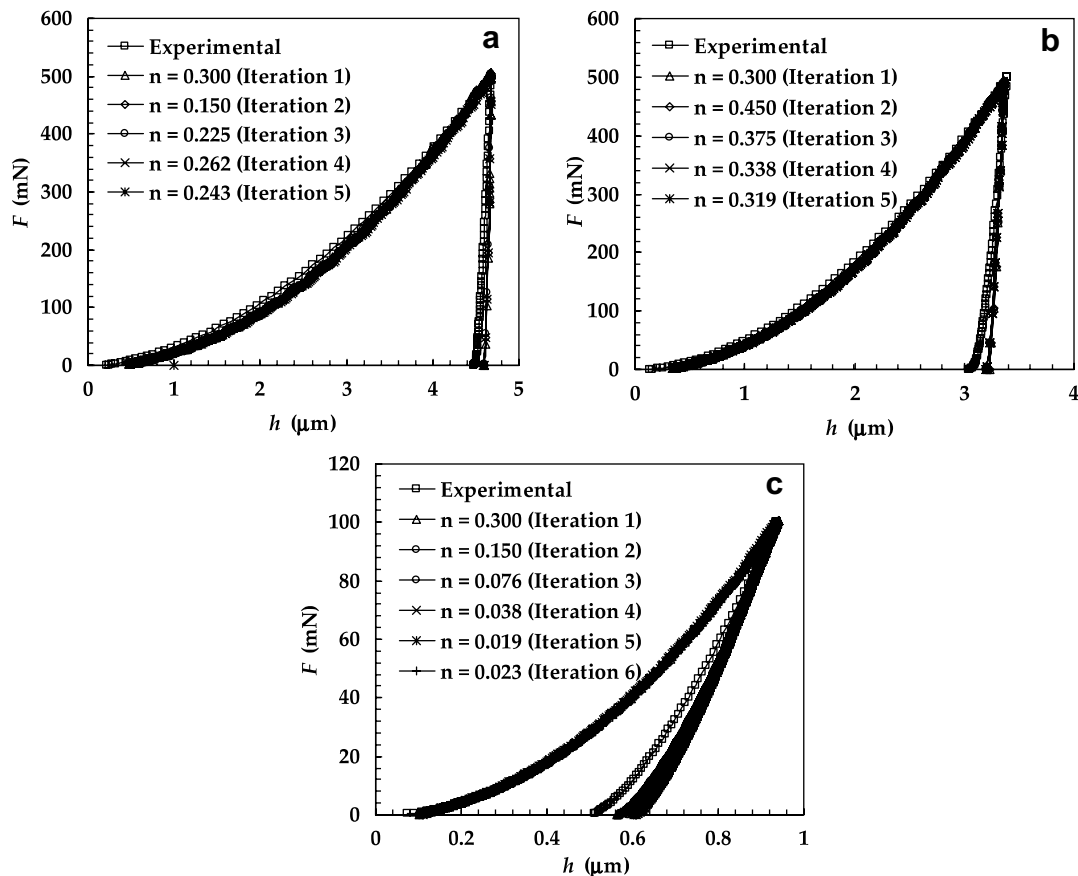| Material	DC 06 steel		AISI 304 steel		BK7 glass	
Algorithm of Fig. 8						
ε_r	0.034		0.034		0.036	
σ_r (GPa)	0.230		0.455		3.464	
	n	σ_y (GPa)	n	σ_y (GPa)	n	σ_y (GPa)
Algorithm of Fig. 12						
Lower limit	0.188	0.153	0.289	0.244	0	3.460
Average	0.243	0.136	0.357	0.227	0.022	3.308
Upper limit	0.298	0.121	0.323	0.211	0.087	2.886

Fig. 15. Experimental and reverse analysis load–indentation depth curves, obtained by using the algorithm shown in Fig. 11: (a) DC 06 steel; (b) AISI 304 steel; and (c) BK7 glass.

The average values, obtained in the experimental hardness tests of each material, for the characteristic parameters of the load–unloading curves, such as the maximum indentation depth, h_{max}, the maximum load, F_{max}, and the stiffness, S, were used as input data in the algorithm of Fig. 8. Table 3 presents the values of the representative stress and strain obtained with this algorithm. In the case of stiffness ($S = 1/C_t$), three different values were considered in the reverse analysis algorithm (Fig. 12), a consequence of the scatter presented by the experimental data. One of them, $S_{average}$, corresponds to the average of the stiffness values of the 25 unloading curves. The two others are related to the limits of stiffness error. These limits were determined by $S_{average} \pm 1.96(St_{dev}/\sqrt{N})$ (where St_{dev} is the standard deviation of S, and N is the number of measurements), corresponding to a risk of 5%. The error of the stiffness ($1.96(St_{dev}/\sqrt{N})$) in relation to the average value ($S_{average}$) obtained for the DC 06 steel, AISI 304 steel and BK7 glass was ±0.9%, ±0.5% and ±0.29%, respectively.

Fig. 15 shows the comparison between the experimental load–unloading curves and the ones obtained by numerical simulations, using the mechanical properties predicted in each iteration of the reverse analysis algorithm given in Fig. 12, for each of the three materials. The experimental load–unloading curves of Fig. 15 correspond to the average of the total curves produced in the hardness tests of each material. For each material, the loading parts of the curves obtained by numerical simulation are similar, and independent of the strain-hardening exponent. All of them show good correlation with the experimental ones. The numerical unloading curves are quite similar to the different strain-hardening exponent values in the case of the steels (Fig. 15a and b for the DC 06 and AISI 304, respectively). For the BK7 glass, the elastic recovery of the numerical unloading curves can easily be seen to increase with increasing values of the strain-hardening exponent (Fig. 15c). However, when stiffness is represented vs. the work-hardening coefficient, a distinction between the unloading curves can be achieved, as shown in Fig. 16.

Fig. 15 shows differences between the unloading curves, experimental and numerical, due to different elastic recoveries. The slightly higher elastic recovery observed in the experimental unloading curves, relative to the numerical results, is related to the compliance of the experimental equipment. The indentation Young's modulus, E, can be obtained from the well-known equations:

$$E_r = \frac{1}{\beta} \frac{\sqrt{\pi}}{2} \frac{1}{\sqrt{A_P}} \frac{1}{(C_t - C_f)}$$
$$\frac{1}{E_r} = \frac{1 - v_s^2}{E} + \frac{1 - v_i^2}{E_i} \tag{8}$$
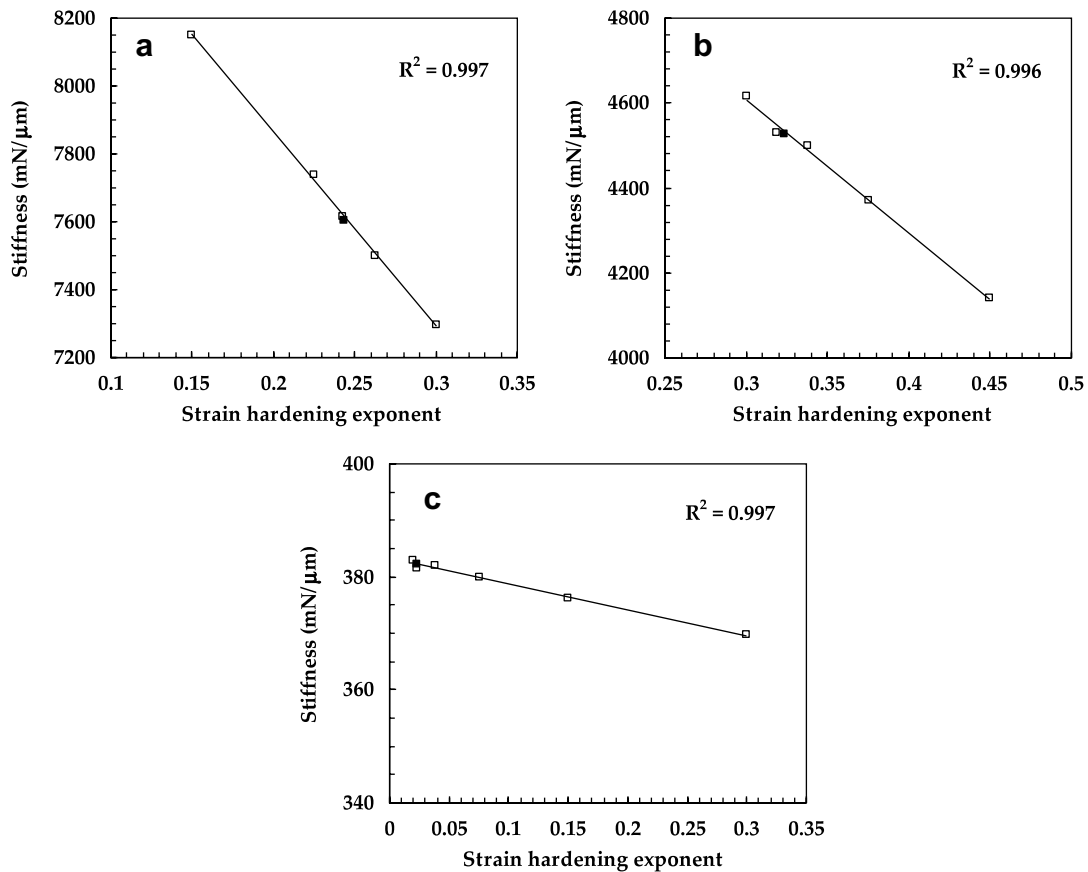

Fig. 16. Stiffness vs. the strain hardening coefficient (open symbols: reverse analysis results; solid symbol: forward analysis): (a) DC 06 steel; (b) AISI 304 steel; and (c) BK7 glass.

where E_r is the reduced Young's modulus, β is the correction factor of the indenter geometry ($\beta = 1.05$, for the Vickers indenter [25]), C_t and C_f are the total compliance of the system and the frame compliance, respectively, and A_P is the contact area; v_s and E are the Poisson ratio and the Young's modulus of the tested material, and v_i and E_i are the Poisson ratio and the Young's modulus of the indenter material. Eq. (8) allows us to write the following equation:

$$C_{exp} = \frac{1}{\beta} \frac{\sqrt{\pi}}{2} \frac{1}{\sqrt{A_{exp}}} \left(\frac{1-v_s^2}{E} + \frac{1-v_i^2}{E_i} \right) + C_f \qquad (9)$$

This equation is applicable to the experimental hardness tests: C_{exp} and A_{exp} correspond to the compliance and the contact area experimentally determined. However, for the case of numerical simulation performed with a rigid indenter, as in this study, the two last terms of the second member of the equation should be zero ($E_i \rightarrow \infty$ and $C_f = 0$) and Eq. (9) becomes (C_{num} and A_{num} are the compliance and the contact area numerically determined):

$$C_{num} = \frac{1-v_s^2}{E} \frac{1}{\beta} \frac{\sqrt{\pi}}{2} \frac{1}{\sqrt{A_{num}}} \qquad (10)$$

So, in order to obtain the same values for the material elastic parameters E and v_s (and so for the ratio $(1 - v_s^2)/E$), the comparison between numerical (C_{num}) and experimen-

tal (C_{exp}) values of the compliance (or the corresponding stiffness values: $S_{num} = 1/C_{num}$ and $S_{exp} = 1/C_{exp}$) needs to take Eqs. (9) and (10) into account:

$$C_{num} = \left(C_{exp} - C_f - \frac{1}{\beta} \frac{\sqrt{\pi}}{2} \frac{1}{\sqrt{A_{exp}}} \frac{1-v_i^2}{E_i} \right) \sqrt{\frac{A_{exp}}{A_{num}}} \qquad (11)$$

Fig. 16 shows the evolution of the numerical stiffness values (open symbols) vs. the strain-hardening exponent for the three materials. As noted above (Fig. 13b), the stiffness values show an evolution in correlation with the strain-hardening exponent, which can be accurately plotted by a straight line. The average stiffness value obtained in the experimental tests, after adjustment using Eq. (11), is also shown (solid symbol) in Fig. 16.

Fig. 17 shows the comparison between the experimental and the corresponding predicted stress–plastic strain curves, obtained with the reverse analysis approach proposed. Errors in the calculation of experimental stiffness result in the upper and lower limits of the stress–strain curve, are both also shown. Table 3 sums up the mechanical properties evaluated with the reverse analysis algorithm for the three materials. A close agreement between the experimental and the average (obtained with the average experimental stiffness) stress–strain curves is obtained. It is clear from the results that the variation ranges of the strain hardening and yield stress values
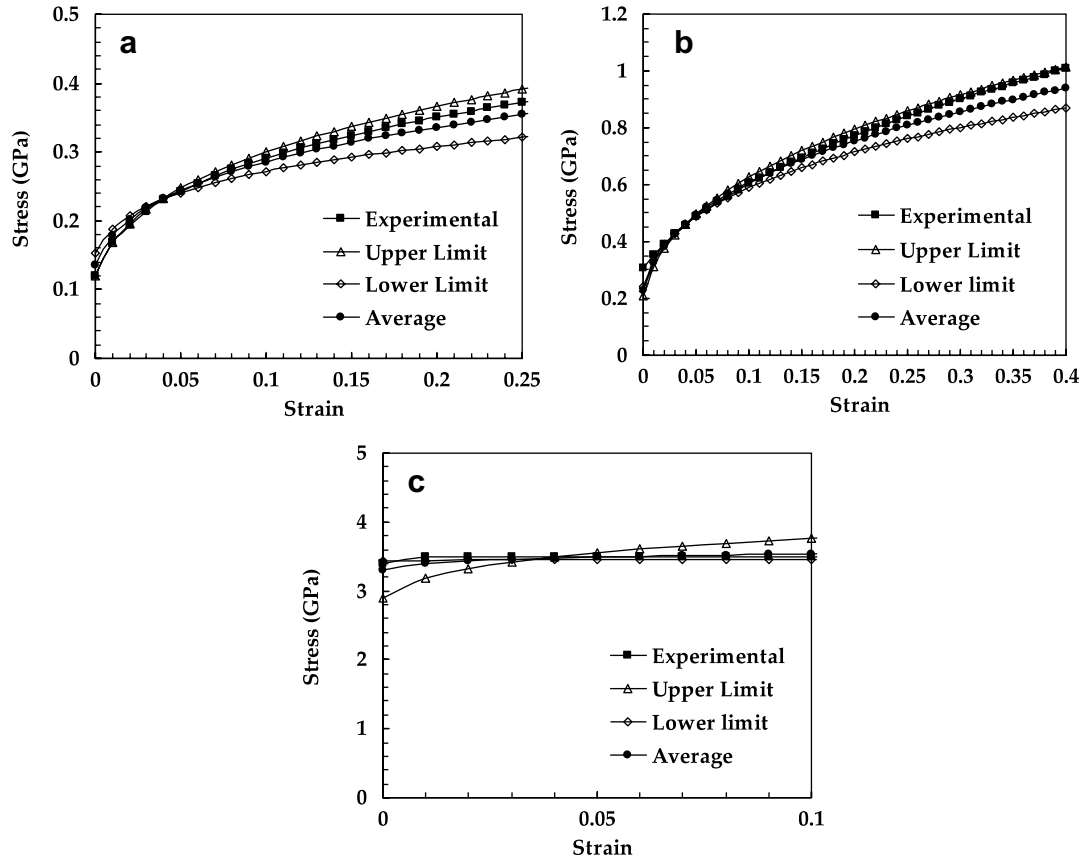

Fig. 17. Comparison between the experimental and predicted reverse analysis stress–strain curves: (a) DC 06 steel; (b) AISI 304 steel; and (c) BK7 glass.

can be minimized by decreasing the experimental stiffness error. In order to achieve such an objective, the recommendations of ISO 14577 [29] must be taken into account.

6. Conclusions

This paper presents a finite element study using the three-dimensional numerical simulation of hardness tests of elastic–plastic materials. The indenter was modulated to account for indenter tip imperfection, as in real cases. In addition, the contact between the Vickers indenter and the deformable body takes friction into account. Forward and reverse analyses were performed in order to extract the plastic properties of materials from the results obtained in depth-sensing indentation tests, using single indenter geometry.

Forward analysis showed that the representative strain depends slightly on the Young's modulus and on the level of the stress–strain curve. We have outlined an empirical relationship that allows the representative stress value to be calculated from the hardness and Young's modulus values. This suggested method for evaluating representative stress can easily be adapted to any indenter geometry.

The numerical reverse analysis allows us, as a first step, to optimize the representative stress value, and thenceforth to predict the values of the strain-hardening exponent and the yield stress. The proposed methodology uses the experimental loading part of the hardness curve, experimentally determined by depth-sensing indentation, to evaluate the representative stress value. The strain-hardening exponent and yield-stress evaluations make use of experimentally determined material stiffness values. The application of the proposed reverse analysis approach to three real materials gives adequate results for the strain hardening and yield stress.

Sensitivity analyses were carried out using forward and reverse analyses. The proposed approach indicates that the strain-hardening coefficient can be very sensitive to the plastic properties of the material, particularly in the cases of materials with low yield stress. However, this methodology ensures uniqueness in all cases, the degree of accuracy being dependent on the range of experimental error in the evaluation of stiffness.

Finally, this reverse analysis approach consists of a straightforward method, which avoids the use of dimensionless functions, determined by fitting polynomial functions to numerical results. We believe that this approach to reverse analysis opens a new modus operandi for reverse analysis in the mechanical characterization of thin films.

References

[1] Doerner MF, Nix WD. J Mater Res 1986;1:601.
[2] Pharr GM, Cook RF. J Mater Res 1990;5:847.
[3] Oliver WC, Pharr GM. J Mater Res 1992;7:1564.
[4] Bolshakov A, Oliver WC, Pharr GM. J Mater Res 1997;11: 760.
[5] Suresh S, Nieh T-G, Choi BW. Scripta Mater 1999;41:951.
[6] Gouldstone A, Koh H-J, Zeng K-Y, Giannakopoulos AE, Suresh S. Acta Mater 2000;48:2277.
[7] Johnson KL. J Mech Phys Solids 1970;18:115.
[8] Suresh S, Alcala J, Giannakopoulos AE. US Patent No. 6,134,954, October 24; 2000.
[9] Dao M, Chollacoop N, Van Vliet KJ, Venkatesh TA, Suresh S, US Provisional Patent, filed with the US Patent Office on March 7; 2001.
[10] Tabor D. The hardness of metals. Oxford: Clarendon Press; 1951.
[11] Laursen YA, Simo JC. J Mater Res 1992;7:618.
[12] Giannakopoulos AE, Larsson P-L, Vestergaard R. Int J Solids Struct 1994;31:2679.
[13] Larsson P-L, Giannakopoulos AE, Soderlund E, Rowcliffe DJ, Vestergaard R. Int J Solids Struct 1996;33:221.
[14] Bolshakov A, Pharr GM. J Mater Res 1998;13:1049.
[15] Cheng Y-T, Li Z. J Mater Res 2000;45:2830.
[16] Jayaraman S, Hahn GT, Oliver WC, Rubin CA, Bastias PC. Int J Solids Struct 1997;35:365.
[17] Chaudhri MM. Acta Mater 1998;46:3047.
[18] Dao M, Chollacoop N, Vliet KJ, Venkatesh TA, Suresh S. Acta Mater 2001;49:3899.
[19] Tho KK, Swaddiwudhipong S, Liu ZS, Zeng K. Mater Sci Eng 2005;390:202.
[20] Chollacoop N, Dao M, Suresh S. Acta Mater 2003;51:3713.
[21] Menezes LF, Teodosiu C. J Mater Process Technol 2000;97: 100.
[22] Antunes JM, Menezes LF, Fernandes JV. In: Covas JA, editor. Proceedings of the second Esaform conference on metal forming, Guimarães; 1999. p. 159.
[23] Menezes LF, Fernandes JV, Trindade A. In: Fritz H-G, editor. Proceedings of the 3rd ESAFORM conference on material forming, Stuttgart. Stuttgart: University of Stuttgart; 2000. p. VII.19.
[24] Simo JC, Laursen TA. Compos Struct 1992;42:97.
[25] Antunes JM, Menezes LF, Fernandes JV. Int J Solids Struct 2006;43:784.
[26] Antunes JM, Cavaleiro A, Menezes LF, Simões MI, Fernandes JV. Surf Coat Technol 2002;149:27.
[27] Casals O, Alcalá J. Acta Mater 2005;53:3545.
[28] European Commission – Standards, Measurements and Testing Programme (SMT). Determination of hardness and modulus of thin films and coatings by nanoindentation – INDICOAT Contract SMT4 – CT98/2249; 1998.
[29] ISO 14577, 2002. Metallic materials – Instrumented indentation tests for hardness and materials parameters. ISO Central Secretariat, Genebra, Suíça.